

Investigating the Formation of MoSe₂ and TiSe₂ Films from Artificially Layered Precursors

Aaron M. Miller, Danielle M. Hamann, Erik C. Hadland, and David C. Johnson*

Cite This: *Inorg. Chem.* 2020, 59, 12536–12544

Read Online

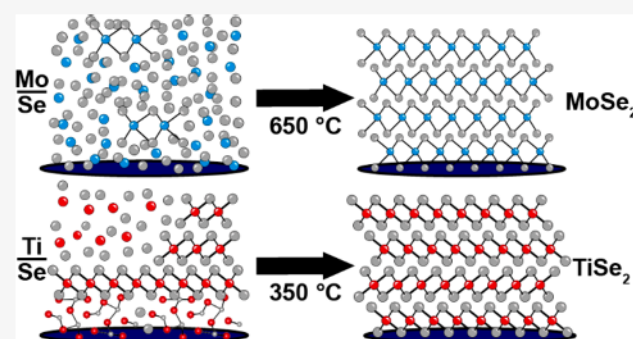
ACCESS |

Metrics & More

Article Recommendations

Supporting Information

ABSTRACT: The reaction of ultrathin layers of Mo and Ti with Se was investigated, and significantly different reaction pathways were found. However, in both systems postdeposition annealing results in smooth dichalcogenide films with specific thicknesses determined by the precursor. X-ray diffraction (XRD) patterns of as-deposited Mo/Se films around a 1:2 ratio of Mo to Se contain weak, broad reflections from small and isolated MoSe₂ crystallites that nucleated during deposition and a sharper intensity maximum resulting from the composition modulation created from the alternating deposition of Mo and Se layers. In contrast, as-deposited Ti/Se films around a 1:2 ratio of Ti to Se contain narrow and intense 00 l reflections from TiSe₂ crystallites and do not contain a Bragg reflection from the sequence of deposited Ti/Se layers. The as-deposited TiSe₂ crystallites have a larger c -axis lattice parameter than was previously reported for TiSe₂, however, which suggests a poor vertical interlayer registry and/or high defect densities including interstitial atoms. In-plane XRD patterns show the nucleation of both TiSe₂ and Ti₂Se during deposition, with the Ti₂Se at the substrate. For both systems, annealing the precursors decreases the peak width and increases the intensity of reflections from crystalline TiSe₂ and MoSe₂. Optimized films consist of a single phase after the annealing and show clear Laue oscillations in the specular XRD patterns, which can only occur if a majority of the diffracting crystallites in the film consist of the same number of unit cells. The highest quality films was obtained when an excess of ~10% Se was deposited in the precursor, which presumably acts as a flux to facilitate diffusion of metal atoms to crystallite growth fronts and compensates for Se loss to the open system during annealing.



INTRODUCTION

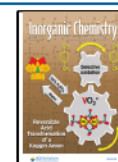
In the 1980s and 1990s, the sequence of solid-state reactions between transition metals deposited on silicon substrates was intensely investigated, because transition-metal silicides were desired as low-resistance replacements for heavily doped polysilicon contacts to transistors in integrated circuits.^{1–3} A focus of this research was understanding the reaction evolution between metals on silicon surfaces, as it was crucial to control the first phase formed in developing the self-aligned silicide or “salicide” process.⁴ The first step in the reaction was proposed to be the formation of an amorphous layer at the interface between the metal and silicon, driven by the enthalpy of mixing of the elements.⁴ Since diffusion rates roughly scale with melting temperatures, the amorphous phase was suggested to have the composition of the lowest melting eutectic in the phase diagram. The compound that is easiest to nucleate from this eutectic was suggested to form first, but there was debate over its identity. Walser and Bene suggested that the congruently melting compound with the highest melting point adjacent to the lowest-melting eutectic would form first. However, a second proposal suggested that the compound with the largest effective heat of formation at the eutectic composition would initially form.⁵ Over time, the concepts developed for metal–silicon reactions were applied to

a broad range of systems, from the formation of amorphous metallic alloys⁶ to the sequence of intermetallic phase formation at reacting metal interfaces.⁷

Recent interest in preparing monolayers of compounds, either alone or as constituents in heterostructures, has focused attention on understanding the formation of ultrathin crystalline layers. Key goals include developing an approach that is scalable to wafer-scale synthesis, capable of controlling thickness to a precise number of unit cells, and able to control defect levels. Thin-film transition-metal dichalcogenides (TMDs) and other layered chalcogenides, due to their diverse and exotic physical properties that can be manipulated by varying the thickness, substrate, or adjacent layers in heterostructures, have attracted significant attention from the two-dimensional (2D) research community.^{8–13} While thickness-dependent properties were initially discovered by cleaving

Received: June 2, 2020

Published: August 12, 2020



bulk samples, subsequent synthesis efforts have focused on developing wafer-scale preparation techniques, such as chemical vapor deposition (CVD).^{14–16} More recently, atomic layer deposition,^{17–19} metal–organic–CVD,^{20–22} and direct deposition methods (sputtering, pulsed laser deposition, e-beam)^{23–25} have been used to make high-quality layered TMDs.²⁶ These approaches use elevated temperatures or light to increase reaction rates, and the quality of the product depends on the temperature and the photon energy utilized (when applicable). The formation process for 2D materials also depends on other process parameters including the structure of the substrate, the pressure, and the carrier and reactant gas fluxes. While plausible chemical schemes have been proposed for many of these systems, there is little reported data of intermediate states and no overarching understanding of how changing reaction parameters impact the formation mechanism.

Here we present X-ray reflectivity (XRR) and X-ray diffraction (XRD) data on the reaction between ultrathin layers of two different metals, Mo and Ti, with amorphous Se. These systems were investigated due to obvious differences in the structure of the as-deposited precursors. The precursors were prepared by sequentially depositing metal and selenium layers on nominally room-temperature substrates. The amount of metal atoms in each of the layers was close to the number required to form a single dichalcogenide layer. For MoSe precursors, nucleation occurs during deposition, but there is little subsequent crystal growth. The as-deposited film, while containing small isolated MoSe₂ crystallites, has a modulated amorphous structure containing alternating Mo-rich and Mo-poor layers. In contrast, the TiSe precursors nucleate both TiSe₂ and Ti₂Se during the deposition. There is no evidence for alternating Ti-rich and Ti-poor layers due to the repeated deposition of the TiSe bilayers. The TiSe₂ grains grow significantly during the deposition of subsequent layers, resulting in an as-deposited film dominated by layers of crystalline TiSe₂. It was experimentally determined that depositing ~10% excess Se in the precursors results in the largest grain sizes for the annealed films for both systems. It is likely that the excess Se not only compensates for the loss of Se to the open system during annealing but also acts as a flux to help facilitate diffusion of the metal atoms during the growth of the crystallites. In summary, these two different dichalcogenides have surprisingly different formation pathways. Annealing precursors with optimized precursor composition and nanoarchitecture at ideal annealing conditions resulted in the formation of layered TiSe₂ and MoSe₂ films with well-defined Laue oscillations, indicating an integral number of unit cells across the entire film.

MATERIALS AND METHODS

Precursors were prepared by repeatedly depositing elemental bilayers of TiSe or MoSe to form an artificially layered precursor. Mo and Ti layers were deposited using an electron-beam gun, while Se was deposited with a Knudsen effusion cell. Precursors were deposited onto silicon substrates with a native oxide layer while maintaining a vacuum of less than 1×10^{-7} Torr during the deposition. In each precursor, the thickness of the Ti and Mo elemental layers was held constant at the thickness required to provide enough metal to form a single Se–M–Se dichalcogenide trilayer. However, the thickness of the Se layer was varied to probe the influence of composition and excess Se on the nucleation and growth of the respective dichalcogenides. In-house deposition software was used to control and monitor the amount of material deposited in each layer using pneumatic-

controlled shutters and quartz crystal microbalances.^{27–30} After deposition, the precursors were removed from the vacuum chamber, briefly exposed to air, and pumped into a drybox, where they were heated in an N₂ environment with less than 1 ppm of O₂ present to crystallize the deposited elemental layers.

Structure and composition were studied via a suite of X-ray techniques. The structures were characterized by X-ray reflectivity (XRR) and X-ray diffraction (XRD), while composition was determined using X-ray fluorescence (XRF). XRR and specular XRD were collected on a Bruker D-8 Discover diffractometer. In-plane XRD was collected on a Rigaku SmartLab diffractometer. All diffraction measurements utilized a copper K α radiation source. The absolute amount of each element deposited was determined using XRF data collected on a Rigaku ZSX Primus II with a rhodium source. Previously published calibration curves were used to relate the background-corrected integrated raw intensity to the atoms/Å² for each element.³¹

RESULTS AND DISCUSSION

The initial structure and evolution of the MoSe₂ precursors during annealing were investigated using XRR and specular XRD. The as-deposited XRR pattern, shown in Figure 1,

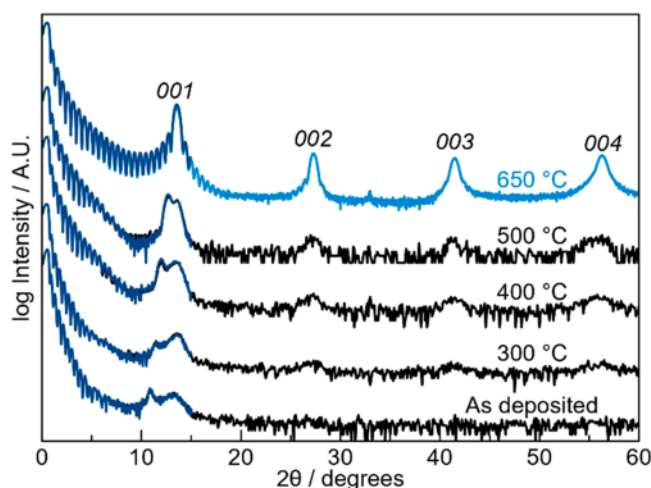


Figure 1. XRR and XRD patterns from an annealing study of an as-deposited MoSe precursor. The annealing temperatures are presented above the scans. XRR scans are from 0–15° 2θ , while XRD scans are from 6–60° 2θ ; the patterns are overlaid and adjusted vertically. All reflections can be indexed to 00l values corresponding to a hexagonal unit cell with lattice parameters consistent with those of MoSe₂.

contains Kiessig fringes, reflecting the total thickness of the deposited films, and two Bragg reflections. The first narrow reflection at $\sim 10.9^\circ 2\theta$ is caused by the artificial layering of the MoSe precursor, yielding a MoSe thickness of 8.1 Å. The total thickness calculated from the Kiessig fringes, 194 Å, is within error of what is expected for a film composed of 24 8.1 Å layers. The disappearance of the Kiessig fringes at $17.8^\circ 2\theta$ indicates that the roughness of the deposited film is on the order of 2.5 Å, which we calculated using the relationship derived by Parratt.³² The broad reflection at $13.4^\circ 2\theta$ corresponds to the first-order Bragg reflection expected for MoSe₂ and indicates that the nucleation and growth of MoSe₂ grains perpendicular to the substrate have occurred during deposition. A potential second-order Bragg reflection, related to the broad reflection at $13.4^\circ 2\theta$, may be present at higher angles but is very weak, suggesting there is significant variation in the distance between crystallized MoSe₂ layers within the grains. Together, the XRR and specular XRD indicate that the

precursor consists of 24 layers containing Mo-rich and Se-rich regions relative to the average composition that are each 8.1 Å thick. Within these layers are small regions that consist of several irregularly stacked MoSe₂ layers forming barely coherent grains of MoSe₂.

The specular XRD patterns evolve gradually as the annealing temperature is increased, and a very crystalline MoSe₂ 00 l diffraction pattern is obtained after being annealed at 650 °C for 60 min. As the annealing temperature is increased, the reflection from artificial layering moves to higher angles, indicating that the period of the artificial layering is becoming smaller. The initial broad reflection at 13.4° 2 θ also shifts to higher angles, becoming narrower and more intense as annealing temperature is increased, indicating that the spread of interlayer distances within each grain is decreasing. This also suggests that there are more MoSe₂ layers within each coherent domain and more MoSe₂ domains in the film. After being annealed at 300 °C, second-, third-, and fourth-order reflections from the MoSe₂ grains are observed, reflecting the increased order within the diffracting domains. These higher-order reflections also increase in intensity and become narrower as annealing temperature is increased, reflecting the increased number and growing size of the MoSe₂ domains. The Kiessig fringes become more intense and extend out to higher angles as annealing temperature is increased, indicating that the film is becoming smoother. Finally, there is considerable growth in intensity and narrowing of diffraction line widths between the 500 and 650 °C annealing steps. The c -axis lattice parameter of the annealed film calculated from the position of the Bragg reflections after the 650 °C annealing is 6.52 Å, which is slightly larger than that previously reported for MoSe₂ (6.460(1) Å).³³ After being annealed at 650 °C, the low-angle reflection from the artificial layering is no longer visible, consistent with the transformation of the precursor from mostly amorphous layers to well-defined crystalline MoSe₂ layers. The Kiessig fringes observed in the XRR scan after being annealed at 650 °C are well-resolved and decay in intensity as expected for a film of uniform electron density and thickness. The presence of both Kiessig fringes and Laue oscillations at higher angles after being annealed at 650 °C indicates that the film becomes significantly smoother and that a constant thickness film with an integer number of MoSe₂ layers occurs across the majority of the substrate. The total film thickness calculated from the positions of the Kiessig fringes is 158 Å, which is within error of that expected for a 24-layer film of MoSe₂ with a c -axis lattice parameter of 6.52 Å. Between the first and second Bragg reflections, Laue oscillations are present. Laue oscillations result from the incomplete destructive interference between Bragg reflections due to a finite number of unit cells. Their presence indicates coherent diffraction from domains in the polycrystalline film that each consist of the same number of MoSe₂ layers. Analysis of the spacing of the Laue fringes indicates that the coherent domains contain 24 MoSe₂ layers, consistent with the number of MoSe bilayers deposited in the precursor and with the total film thickness.

In-plane diffraction data were collected for the MoSe film annealed at 650 °C and are shown in Figure 2. All observed reflections can be indexed to a hexagonal unit cell with an a -axis lattice parameter of 3.31(1) Å. This is slightly larger than what has been previously reported for bulk MoSe₂ (3.289(1) Å)³³ and MoSe₂ thin films (3.246 Å).³⁴ The composition and diffraction data provide consistent evidence that the crystallized material is MoSe₂.

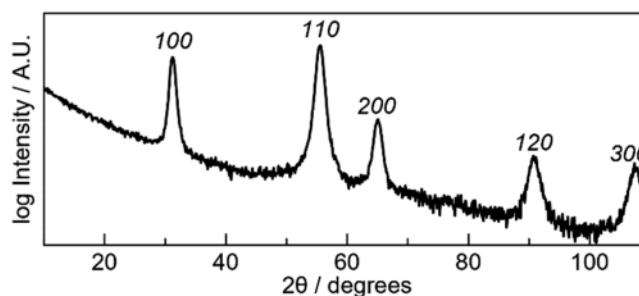


Figure 2. Grazing incidence in-plane diffraction of a MoSe₂ film after being annealed at 650 °C for 60 min. All reflections can be indexed as $hk0$ reflections (shown above each reflection) corresponding to a hexagonal unit cell with lattice parameters consistent with those of MoSe₂.

MoSe precursors with different amounts of Se were annealed at 650 °C and characterized by XRD to probe the influence of composition on the growth and crystallinity of the final product. Figure 3 graphs the intensity and peak width of

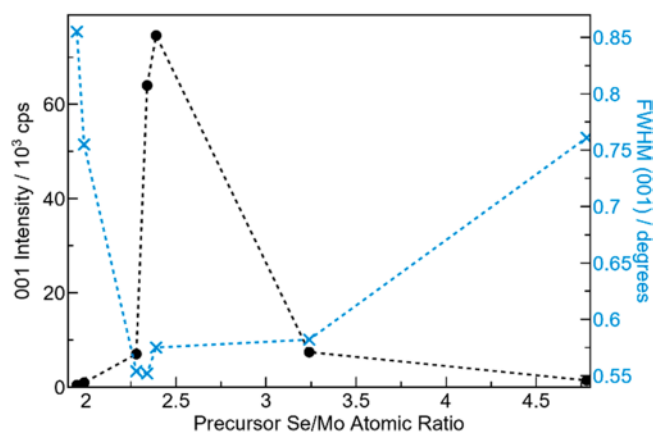


Figure 3. MoSe₂ crystal quality as determined by specular diffraction reflection intensity and peak width graphed vs the composition of the MoSe precursor.

the 001 reflection of MoSe₂ as a function of the Se content in the precursor prior to being annealed. The peak width of the 00 l reflections depends on the size and coherence of the MoSe₂ layers along the c -axis, with a minimum peak width occurring when the entire film thickness consists of a single coherent domain. The data in Figure 3 demonstrate that some excess Se is required to obtain the narrowest line widths, but too much excess increases the line width. The intensity of the 00 l reflections is proportional to the number of MoSe₂ domains that are aligned parallel to the substrate, and the maximum intensity was observed for annealed films that began with a 10–15% excess of Se. Rocking curves taken on these samples are narrowest for those with the highest intensity of the 001 reflection, suggesting that the intensity maximum is due to the percentage of the sample that is crystallographically aligned. The variation of crystalline quality with Se concentration is likely caused by the excess Se acting as a flux, increasing the mobility of the Mo cations during annealing. However, too much Se results in the nucleation of grains of MoSe₂ that are not aligned with the basal plane perpendicular to the substrate, preventing the entire film thickness from becoming a single coherent domain.

Table 1. Structure and Composition Summary for the As-Deposited TiSe Precursors

No. of TiSe layers deposited	total film thickness (Å, ± 0.5)	average bilayer thickness (Å)	average Ti atoms, Å ² per bilayer (±0.07)	average Se atoms, Å ² per bilayer (±0.04)	composition Ti/Se	as-deposited TiSe ₂ c-axis lattice parameter (Å, ± 0.01)
83	478	5.8	0.092	0.185	1:2.01	6.14
83	487	5.9	0.092	0.188	1:2.05	6.17
83	507	6.1	0.094	0.198	1:2.11	6.16
84	509	6.1	0.089	0.192	1:2.14	6.17
83	524	6.3	0.092	0.198	1:2.16	6.19
84	527	6.3	0.089	0.197	1:2.22	6.19
82	482	5.8	0.084	0.188	1:2.24	6.18
83	532	6.4	0.090	0.204	1:2.26	6.20
84	564	6.7	0.082	0.210	1:2.57	6.27

A series of TiSe precursors with various Ti/Se ratios were prepared to compare their evolution to that found for MoSe precursors forming MoSe₂. Table 1 summarizes data obtained from each of the TiSe precursors. The XRF data show that all precursors were Se rich as-deposited, and the number of Ti atoms/Å² deposited per TiSe bilayer ranged from 2% above to 10% below the number required for a single ideal crystalline TiSe₂ trilayer, 0.092 Ti atoms/Å². The total thicknesses for the samples were calculated from the Kiessig fringes and divided by the number of TiSe bilayers that were deposited to obtain the average TiSe bilayer thickness for each sample (Table 1). The thicknesses are consistent with the number of atoms deposited calculated from the XRF intensities (Table 1). The specular diffraction patterns of the as-deposited precursors all contain two to four 00*l* reflections from the crystalline TiSe₂ domains (see Figure 5), indicating that the as-deposited films are much more crystalline than the corresponding MoSe films. The *c*-axis lattice parameters were all larger than those previously reported for TiSe₂, reflecting the high defect levels resulting from the low ambient temperature during the deposition. There is a systematic increase in the *c*-axis lattice parameter as the amount of Se deposited in the sample increases, suggesting that interstitial Se atoms may be trapped between layers due to limited diffusion at these low annealing temperatures. The in-plane diffraction patterns (shown in black in Figures 5 and S2) also reflect the more crystalline nature of the as-deposited TiSe films, containing reflections that can be indexed as *hk*0 reflections from TiSe₂ and broad reflections consistent with the presence of Ti₂Se deposited, and the number of Ti atoms/Å² deposited per TiSe bilayer ranged from 2% above to 10% below the number required for a single ideal crystalline TiSe₂ trilayer, 0.092 Ti atoms/Å². The as-deposited XRR patterns (Figure S1) contained Kiessig fringes, reflecting the total thickness of the deposited films and a strong first-order reflection from crystalline TiSe₂. The disappearance of the Kiessig fringes at 7.4° 2θ indicates that the roughness of the deposited film is on the order of 6 Å, which we calculated using the relationship derived by Parratt.³² Unlike the MoSe precursors, no reflection intensity was observed that could be attributed to the artificial layering of the TiSe precursors.

Taken together, the diffraction data indicate that the TiSe precursors substantially interdiffuse and react during deposition. Since the film's overall compositions are Se-rich, we suspect that the observed Ti₂Se is formed during the deposition when Se is deposited on top of the initial Ti layer. After the first TiSe bilayer is deposited, TiSe₂ nucleates, either at the surface of the Se layer or at the Ti₂Se surface below, by diffusing through the amorphous Se layer. When subsequent layers are deposited, Ti atoms must diffuse through

the Se-rich matrix to the growth fronts of existing TiSe₂ crystallites. When this diffusion length becomes sufficiently large, new crystalline layers of TiSe₂ may nucleate near the surface of the sample. The reactions during the deposition result in large regions of crystalline TiSe₂ surrounded by a Se-rich matrix, with Ti₂Se adjacent to the Si substrate.

Figure 4 contains a series of XRR and XRD patterns collected as a function of the annealing temperature for a

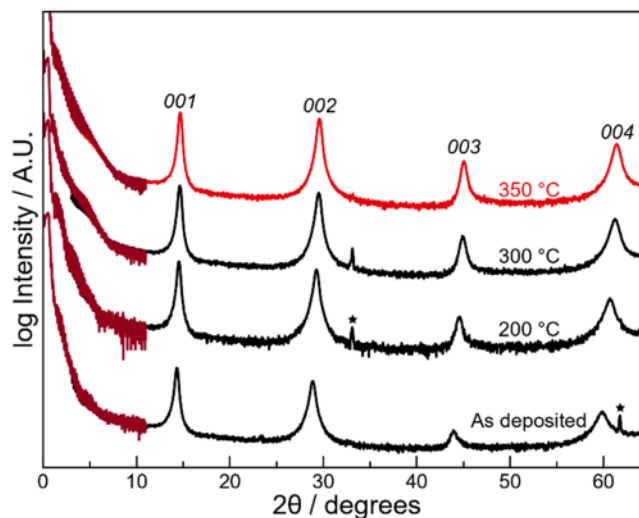


Figure 4. XRR and XRD patterns from an annealing study of an as-deposited TiSe precursor with a starting composition of 1:2.24 (Ti/Se). The sample was annealed for 30 min at the temperatures presented above each scan. XRR scans are from 0–11° 2θ, while XRD scans are from 3–65° 2θ; the patterns are overlaid and adjusted vertically. All reflections can be indexed to 00*l* values corresponding to a hexagonal unit cell with lattice parameters consistent with TiSe₂. Reflections marked with an asterisk correspond to the substrate.

representative TiSe precursor with an initial Ti/Se composition of 1:2.24. The 00*l* reflections of the TiSe₂ crystallites move noticeably to a higher angle as the annealing temperature is increased, indicating a decrease in the *c*-axis lattice parameter. Additionally, the reflection intensity increases while the line widths (full width at half-maximum (fwhm)) decrease as the annealing temperature is increased, suggesting the registration between the TiSe₂ planes increases excess atoms between layers and at grain boundaries are incorporated into the growing crystallites or diffuse to the surface. In all but the least Se-rich films, the in-plane reflections of Ti₂Se become unobservable. However, Ti₂Se in-plane reflections remain after being annealed in the most Ti-rich film studied. Films

Table 2. Compositions and Lattice Parameters for Annealed TiSe Films As Determined from Full Pattern XRD Le Bail Fits

AD composition (Ti/Se)	annealed total film thickness (Å)	<i>c</i> -lattice parameter (Å)	<i>a</i> -lattice parameter (Å)	annealed expt Ti atoms, Å ² (±0.08)	annealed expt Se atoms, Å ² (±0.02)	annealed composition (Ti/Se)
1:2.01	479	6.053(1)	3.551(1)	7.54	15.05	1:2.00
1:2.05	479	6.051(1)	3.558(1)	7.57	15.21	1:2.01
1:2.11	503	6.050(1)	3.559(1)	7.86	15.46	1:1.97
1:2.14	483	6.034(1)	3.558(1)	7.70	14.41	1:1.87
1:2.16	501	6.037(1)	3.560(1)	7.70	15.49	1:2.01
1:2.22	503	6.043(1)	3.553(1)	7.70	15.35	1:1.99
1:2.24	450	6.066(1)	3.549(1)	6.86	12.85	1:1.87
1:2.26	496	6.058(1)	3.554(1)	7.50	15.10	1:2.01
1:2.57	505	6.096(1)		6.80	13.80	1:2.03

annealed at 350 °C have the greatest reflection intensity and narrowest peak widths. Annealing above 350 °C results in a decrease in intensity and an increase in peak width of the 00*l* reflections. On the basis of the above observations, the optimal annealing temperature for the TiSe precursors was determined to be 350 °C.

As was done in the MoSe system, precursor films were prepared by holding the thickness of the Ti layer constant, varying the amount of Se, and annealing under identical conditions (350 °C for 30 min) to study the effects of precursor composition on film quality. For all the films, the XRF data show that Se was lost during annealing (Table 2). The XRR patterns, shown in Figures S1 and S3, all contain Kiessig fringes from the interference of the front and back of the film. In contrast to the MoSe system, the surface roughness of the films does not change significantly during annealing. Because of the loss of Se during the annealing, all the annealed films are thinner than the as-deposited precursors. Oscillations in the intensity of the Kiessig fringes in all the films indicate that a surface layer with a different electron density than the rest of the sample has formed, likely a surface layer of amorphous TiO₂. This oxide layer forms during annealing in an inert atmosphere with less than 1 ppm of O₂ present. This may seem surprising until recognizing that, despite the low oxygen concentration present, approximately a monolayer's worth of O₂ molecules impacts the film during each second of annealing.

The annealed XRR patterns fall into two general categories—those with a thicker (~50 Å) TiO₂ layer and those with a thinner (~10 Å) TiO₂ layer on top of the film (Figure S4). The specular diffraction patterns (Figures 5a and S2a) contain 00*l* reflections from crystalline TiSe₂. The observed reflections are more intense, narrower, and occur at higher 2θ angles than those in the as-deposited precursors, indicating there are more 00*l* planes aligned with the substrate, the TiSe₂ crystalline domains are thicker, and that the *c*-axis lattice parameters are smaller. The *c*-axis lattice parameters obtained from full pattern Le Bail fits are summarized in Table 2. Samples that have a slight excess of Se, in the composition range between 1:2.14 and 1:2.22 on deposition, have *c*-axis lattice parameters that best match the reported values for TiSe₂. Films with initial compositions on either side of this regime have *c*-axis lattice parameters that are slightly larger than the literature value. Representative in-plane XRD patterns for the films are shown in Figures 5b and S2b. The annealed patterns have narrower reflections than those found in the as-deposited samples, indicating a significant increase in the in-plane domain size. All of the reflections in the annealed samples can be indexed to a hexagonal unit cell with lattice

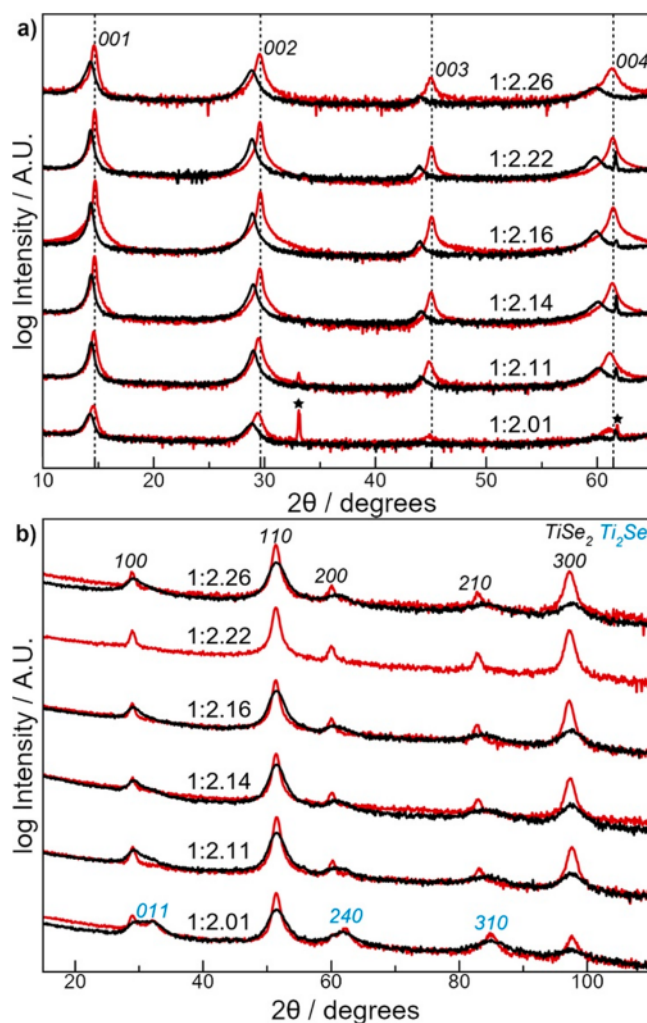


Figure 5. Representative specular (a) and in-plane (b) XRD patterns of TiSe thin films with various compositions. Black curves show the diffraction pattern of the precursor, while red curves show the pattern for the films annealed at 350 °C. All observed reflections that correspond to the TiSe₂ crystal structure are indexed in black. Reflections marked with an asterisk observed in the specular pattern are attributed to the Si substrate. Reflections for the observed Ti₂Se impurity phase are indexed in blue. Additional diffraction patterns can be found in Figure S2.

parameters similar to the reported values for TiSe₂ (Table 2), except for broad reflections in the 1:2.01 sample, which correspond to an impurity phase of Ti₂Se.³⁵ This phase also appears to be present to some extent in all precursors prior to being annealed. The *a*-axis lattice parameters for all of the Ti

Se films, determined from the Le Bail fits of the in-plane diffraction patterns found in Figure 5b, are very similar to those previously reported for TiSe_2 (Table 2).³⁵ Unlike the c -axis lattice parameters, which were influenced by the amount of Se present in the precursor sample, the a -axis lattice parameter for the annealed TiSe_2 films does not depend on the precursor composition.

The change in the crystallinity of the TiSe_2 films as a function of precursor composition was estimated by using the line widths of the specular and in-plane reflections in the diffraction patterns of the annealed precursors. Line widths of the 110 and 001 reflections in the in-plane and specular XRD patterns, respectively, were determined to help quantify the effect of precursor composition on crystal quality (Figure 6).

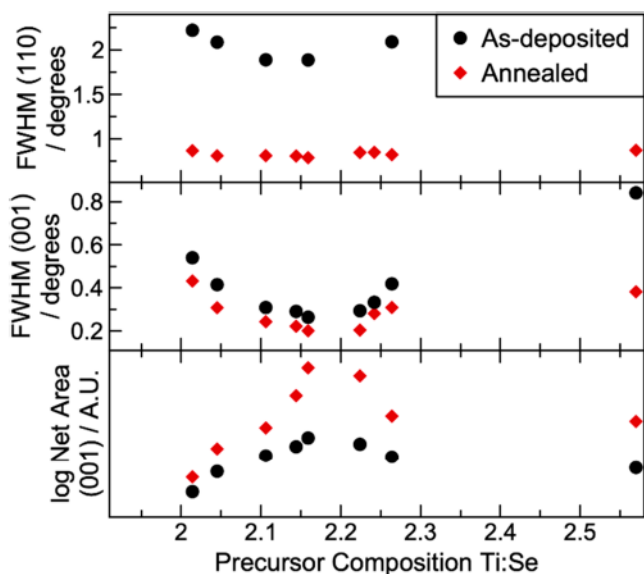


Figure 6. Line widths (fwhm) of the 110 reflection in the in-plane XRD pattern (top) and 001 reflection in the specular XRD pattern (middle) and 001 reflection net area (bottom) as a function of precursor composition. (●) As-deposited parameters. (◆) Annealed parameters. The diffraction patterns used to determine these parameters are found in Figure 4 and Figure S2.

In the as-deposited films, both specular and in-plane line widths are smallest when the precursors have a Ti/Se ratio of 1:2.15–1:2.2. After being annealed, both the in-plane and specular diffraction patterns have the smallest line widths (and largest crystallite sizes) at a Se/Ti ratio of ~ 2.15 – 2.2 ; however, there is a much smaller range of in-plane line widths. A Scherrer analysis of the line widths for the sample with an as-deposited composition of 1:2.16 yields a c -axis crystallite size of 443 Å and an in-plane crystallite size of 117 Å. Similar to what was observed in the MoSe system, it is possible that the slight excess of Se acts as a flux to facilitate the transport of Ti atoms to the crystallite growth fronts, causing larger crystallite sizes in precursors with the ideal amount of excess Se. For the three TiSe_2 samples with the optimal amount of excess Se to obtain large coherent diffracting domains, Laue oscillations are visible surrounding the first Bragg reflection (Figure 7). The Laue oscillations occur due to the incomplete destructive interference of a finite number of unit cells in a crystal. For a small number of unit cells N , the Laue function, $\sin(Nx)/\sin(x)$, results in a principle intensity maximum whose position is determined by the lattice parameters of the diffracting crystal

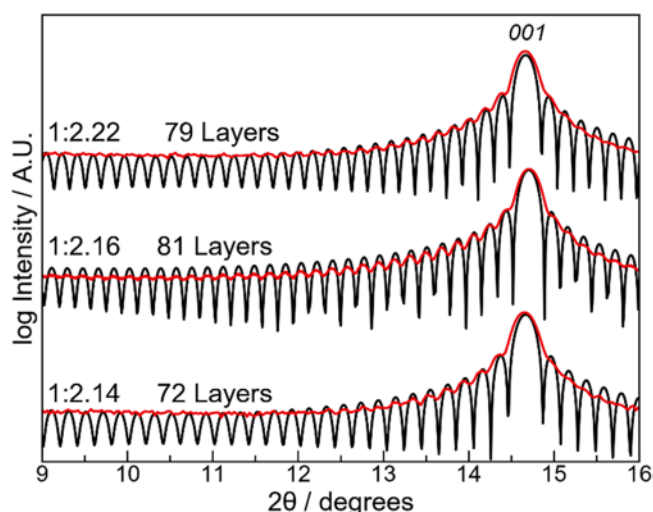


Figure 7. Experimental specular XRD patterns (red) for the highest-quality annealed TiSe_2 films overlaid with the theoretical Laue oscillations expected for n layers of TiSe_2 (black).

and a series of evenly spaced maxima on either side whose spacing is determined by the number of unit cells in the crystal. To observe the Laue oscillations, the majority of the film must consist of crystallites with identical numbers of unit cells, because crystallites with different numbers of unit cells would contribute Laue intensities at different angles, destroying the interference pattern. Figure 7 shows the measured specular diffraction pattern around the first Bragg reflection for the annealed samples with Laue oscillations. The position of the highest intensity maxima is consistent with the c -axis lattice parameters given in Table 2. The spacing of the Laue oscillations is consistent with the diffracting crystallites having a specific number of unit cells, as shown by the simulated patterns overlaid on the experimental patterns in Figure 7. However, the total film thicknesses of these annealed samples are larger than the product of the number of unit cells calculated from the Laue oscillations multiplied by the appropriate c -axis lattice parameter. Since the number of Ti/Se bilayers deposited in the precursors was larger than the number of layers formed, there is more Ti in the samples than required for the number of TiSe_2 layers calculated from the Laue oscillations. This suggests that several Ti/Se bilayers were oxidized, formed Ti_2Se , and/or reacted with the substrate.

The combination of XRF, XRR, and XRD data allows us to speculate on an atomic-level picture of the structure of the as-deposited MoSe and TiSe precursors and how it evolves during annealing. Analysis of the diffraction data clearly indicates that the structure of the as-deposited Mo and Ti precursors are significantly different, which is illustrated schematically in Figure 8. The MoSe precursor, Figure 8a, has a composition modulation from the growth of the sequence of as-deposited layers with small crystallites of MoSe_2 several layers thick distributed throughout the film. Figure 8c illustrates how the TiSe precursor has reacted much more during deposition than the MoSe precursor. In the TiSe precursors, there is no evidence of compositional modulation; Ti_2Se forms during the deposition of Se on the first layer of Ti deposited, and thick domains of poorly stacked TiSe_2 layers subsequently grow during the deposition. In both the MoSe and TiSe precursors, there is a gradient in metal concentration around the growth front as it is depleted around each

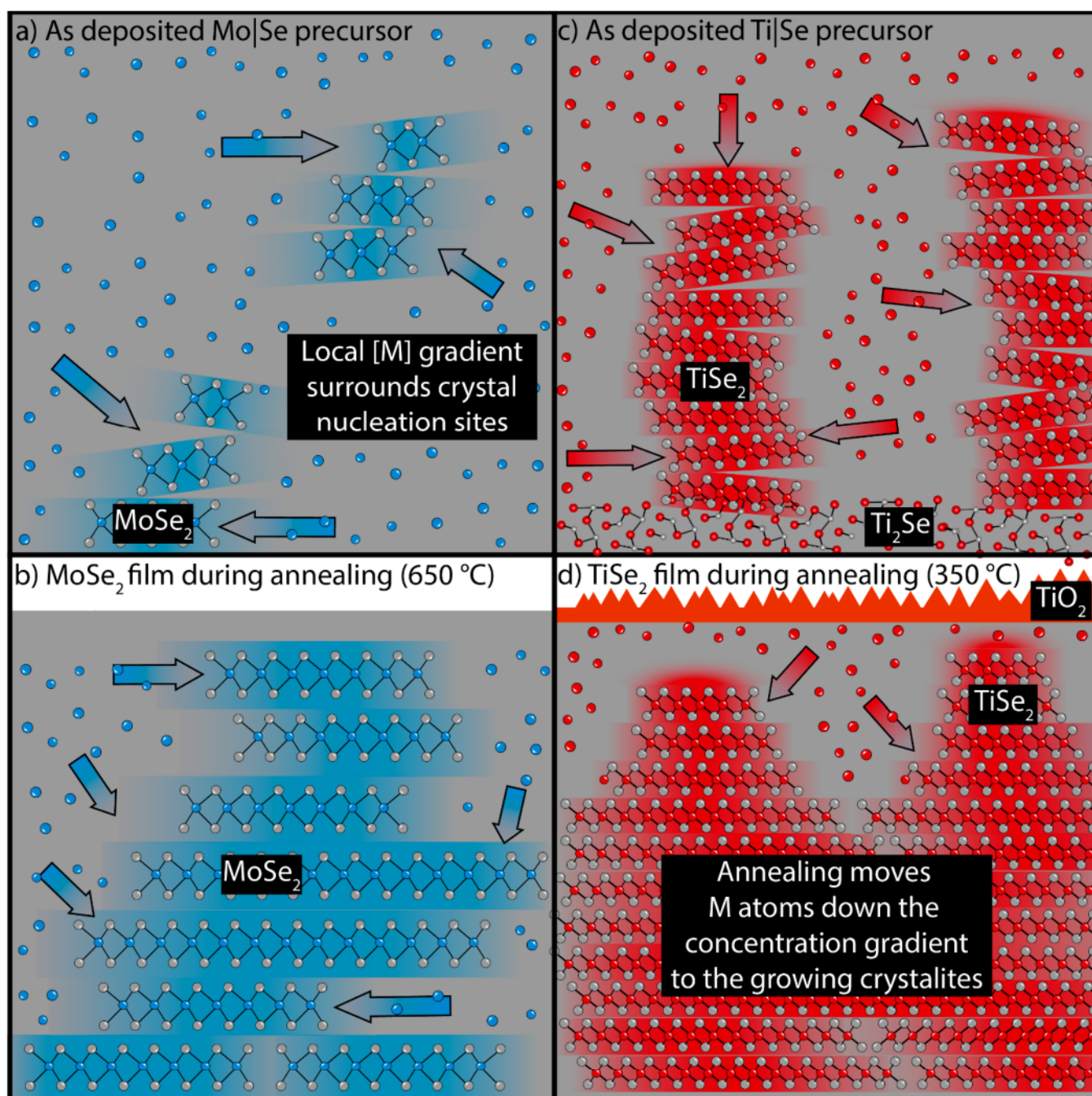


Figure 8. Proposed atomic-level pictures for the evolution of Mo|Se (a) and Ti|Se (c) precursors as they are annealed to form crystalline MoSe₂ (b) and TiSe₂ (d). There is much more interdiffusion during deposition of the lighter Ti atoms, resulting in larger crystalline domains in the as-deposited TiSe₂ precursor relative to the Mo|Se precursor.

crystallite. For the Mo|Se precursor, the concentration gradient is not enough to induce diffusion during the deposition, likely a result of the high activation energies required for diffusion. However, in the Ti|Se precursors, smaller Ti atoms diffuse significantly during deposition to form the observed thick TiSe₂ domains. In both systems, annealing at elevated temperatures allows more diffusion to occur, leading to the growth of well-organized crystallites. A small amount of excess Se (10%) results in the formation of larger coherent domains of the dichalcogenide in both systems. The excess Se presumably acts as a flux to increase the rate of diffusion of the metal cations. However, too much excess Se results in less

crystallographically aligned layers and smaller grain sizes. In both systems, the optimized precursor structure and annealing temperatures resulted in the formation of polycrystalline films that predominantly contained a precise and identical number of dichalcogenide planes. For Mo|Se films with the correct amount of Mo per Mo|Se bilayer in the precursor, each Mo|Se layer evolved into a single MoSe₂ trilayer plane in the coherent domain. In analogous Ti|Se films, all of the Ti|Se layers evolved into TiSe₂ except for two layers at the surface of the film that oxidized, forming a TiO₂ surface layer.

CONCLUSIONS

Highly crystalline transition-metal diselenide films can be prepared by depositing alternating layers of the metal and selenium. With the correct amount of metal and a slight excess of Se deposited per MSe bilayer, each layer will evolve into a dichalcogenide plane upon annealing. This enables the thickness of the dichalcogenide film to be controlled to a specified number of unit cells over large areas. While a precise number of dichalcogenide planes was obtained in both the Ti–Se and Mo–Se systems, the reaction pathways were very different. TiSe₂ mostly self-assembles during the deposition process, while MoSe₂ mostly self-assembles during annealing. In both systems, concentration gradients drive the diffusion of metals to the crystallite growth fronts, aided by the short diffusion distances in the layered precursor during annealing or surface diffusion during the deposition. The diffraction data gathered on the as-deposited films and during annealing enabled the creation and comparison of atomistic pictures describing the self-assembly of MoSe₂ and TiSe₂ from their respective precursors. By understanding the film formation and developing control over the composition and morphology of the precursors, we demonstrate that growth of dichalcogenides can be controlled to achieve uniform thicknesses over large areas.

ASSOCIATED CONTENT

Supporting Information

The Supporting Information is available free of charge at <https://pubs.acs.org/doi/10.1021/acs.inorgchem.0c01626>.

XRR patterns as a function of temperature, additional specular and in-plane XRD patterns for as-deposited and annealed TiSe₂ films, XRR patterns for all annealed TiSe₂ films, and simulated and experimental XRR patterns showing the effect of oxide growth (PDF)

AUTHOR INFORMATION

Corresponding Author

David C. Johnson – Department of Chemistry and Biochemistry, University of Oregon, Eugene, Oregon, United States; orcid.org/0000-0002-1118-0997; Email: davej@uoregon.edu

Authors

Aaron M. Miller – Department of Chemistry and Biochemistry, University of Oregon, Eugene, Oregon, United States; orcid.org/0000-0003-0493-9464

Danielle M. Hamann – Department of Chemistry and Biochemistry, University of Oregon, Eugene, Oregon, United States; orcid.org/0000-0002-9262-1060

Erik C. Hadland – Department of Chemistry and Biochemistry, University of Oregon, Eugene, Oregon, United States

Complete contact information is available at: <https://pubs.acs.org/doi/10.1021/acs.inorgchem.0c01626>

Author Contributions

The manuscript was written through contributions of all authors. All authors have given approval to the final version of the manuscript.

Notes

The authors declare no competing financial interest.

ACKNOWLEDGMENTS

The authors acknowledge support from the National Science Foundation (NSF) under Grant No. DMR-1710214. This material is based in part upon work supported by the NSF Graduate Research Fellowship Program under Grant No. 1309047. We acknowledge the Center for Advanced Materials Characterization in Oregon at the University of Oregon.

REFERENCES

- (1) Mayer, J. W.; Tu, K. N. Analysis of Thin-Film Structures with Nuclear Backscattering and x-Ray Diffraction. *J. Vac. Sci. Technol.* 1974, 11, 86.
- (2) Krautle, H.; Nicolet, M.-A.; Mayer, J. W. Kinetics of Silicide Formation by Thin Films of V on Si and SiO₂ Substrates. *J. Appl. Phys.* 1974, 45, 3304.
- (3) Mayer, J. W.; Poate, J. W.; Tu, K. N. Thin Films and Solid-Phase Reactions. *Science* 1975, 190, 228.
- (4) Walser, R. M.; Bene, R. W. First Phase Nucleation in Silicon-Transition-Metal Planar Interfaces. *Appl. Phys. Lett.* 1976, 28, 624.
- (5) Pretorius, R.; Theron, C. C.; Vantomme, A.; Mayer, J. W. Compound Phase Formation in Thin Film Structures. *Crit. Rev. Solid State Mater. Sci.* 1999, 24, 1–62.
- (6) Cotts, E. J.; Meng, W. J.; Johnson, W. L. Calorimetric Study of Amorphization in Planar, Binary, Multilayer, Thin-Film Diffusion Couples of Ni and Zr. *Phys. Rev. Lett.* 1986, 57, 2295.
- (7) Clemens, B. M.; Sinclair, R. Metastable Phase Formation in Thin Films and Multilayers. *MRS Bull.* 1990, 15 (2), 19–28.
- (8) Schneider, L. M.; Lippert, S.; Renaud, D.; Kuhnert, J.; Kang, K. N.; Ajayi, O.; Halbich, M. U.; Abdulmunem, O. M.; Lin, X.; Hassoon, K.; Edalati-Boostan, S.; Kim, Y. D.; Heimbrodt, W.; Yang, E. H.; Hone, J. C.; Rahimi-Iman, A. Influence of the Substrate Material on the Optical Properties of Tungsten Diselenide Monolayers. *2D Mater.* 2017, 4, 025045.
- (9) Niu, Y.; Gonzalez-Abad, S.; Frisenda, R.; Marauhn, P.; Drüppel, M.; Gant, P.; Schmidt, R.; Taghavi, N. S.; Barcons, D.; Molina-Mendoza, A. J.; de Vasconcelos, S. M.; Bratschitsch, R.; Perez De Lara, D.; Rohlfing, M.; Castellanos-Gomez, A. Thickness-Dependent Differential Reflectance Spectra of Monolayer and Few-Layer MoS₂, MoSe₂, WS₂ and WSe₂. *Nanomaterials* 2018, 8 (9), 725.
- (10) Hamann, D. M.; Lygo, A. C.; Esters, M.; Merrill, D. R.; Ditto, J.; Sutherland, D. R.; Bauers, S. R.; Johnson, D. C. Structural Changes as a Function of Thickness in [(SnSe)_{1+δ}]_m TiSe₂ Heterostructures. *ACS Nano* 2018, 12, 1285.
- (11) Biswas, R. K.; Khan, P.; Mukherjee, S.; Mukhopadhyay, A. K.; Ghosh, J.; Muraleedharan, K. Study of Short Range Structure of Amorphous Silica from PDF Using Ag Radiation in Laboratory XRD System, RAMAN and NEXAFS. *J. Non-Cryst. Solids* 2018, 488, 1–9.
- (12) Hamann, D. M.; Merrill, D. R.; Bauers, S. R.; Mitchson, G.; Ditto, J.; Rudin, S. P.; Johnson, D. C. Long-Range Order in [(SnSe)_{1.2}]₁[TiSe₂]₁ Prepared from Designed Precursors. *Inorg. Chem.* 2017, 56 (6), 3499–3505.
- (13) Li, L. J.; O'Farrell, E. C. T.; Loh, K. P.; Eda, G.; Özyilmaz, B.; Castro Neto, A. H. Controlling Many-Body States by the Electric-Field Effect in a Two-Dimensional Material. *Nature* 2016, 529 (7585), 185–189.
- (14) Novoselov, K. S.; Geim, A. K.; Morozov, S. V.; Jiang, D.; Zhang, Y.; Dubonos, S. V.; Grigorieva, I. V.; Firsov, A. A. Electric Field Effect in Atomically Thin Carbon Films. *Science (Washington, DC, U. S.)* 2004, 306, 666–669.
- (15) Wang, X.; Gong, Y.; Shi, G.; Chow, W. L.; Keyshar, K.; Ye, G.; Vajtai, R.; Lou, J.; Liu, Z.; Ringe, E.; Tay, B. K.; Ajayan, P. M. Chemical Vapor Deposition Growth of Crystalline Monolayer MoSe₂. *ACS Nano* 2014, 8 (5), 5125–5131.
- (16) Lu, X.; Utama, I. B.; Lin, J.; Gong, X.; Zhang, J.; Zhao, Y.; Pantelides, S. T.; Wang, J.; Dong, Z.; Liu, Z.; Zhou, W.; Xiong, Q. Large-Area Synthesis of Monolayer and Few-Layer MoSe₂ Films on SiO₂ Substrates. *Nano Lett.* 2014, 14 (5), 2419–2425.

- (17) Tan, L. K.; Liu, B.; Teng, J. H.; Guo, S.; Low, H. Y.; Loh, K. P. Atomic Layer Deposition of a MoS₂ Film. *Nanoscale* 2014, 6 (18), 10584–10588.
- (18) Song, J.-G.; Park, J.; Lee, W.; Choi, T.; Jung, H.; Lee, C. W.; Hwang, S.-H.; Myoung, J. M.; Jung, J.-H.; Kim, S.-H.; Lansalot-Matras, C.; Kim, H. Layer-Controlled, Wafer-Scale, and Conformal Synthesis of Tungsten Disulfide Nanosheets Using Atomic Layer Deposition. *ACS Nano* 2013, 7 (12), 11333–11340.
- (19) Jin, Z.; Shin, S.; Kwon, D. H.; Han, S.-J.; Min, Y.-S. Novel Chemical Route for Atomic Layer Deposition of MoS₂ Thin Film on SiO₂/Si Substrate. *Nanoscale* 2014, 6 (23), 14453–14458.
- (20) Kang, K.; Xie, S.; Huang, L.; Han, Y.; Huang, P. Y.; Mak, K. F.; Kim, C. J.; Muller, D.; Park, J. High-Mobility Three-Atom-Thick Semiconducting Films with Wafer-Scale Homogeneity. *Nature* 2015, 520, 656–660.
- (21) Eichfeld, S. M.; Hossain, L.; Lin, Y.-C.; Piasecki, A. F.; Kupp, B.; Birdwell, A. G.; Burke, R. A.; Lu, N.; Peng, X.; Li, J.; Azcatl, A.; McDonnell, S.; Wallace, R. M.; Kim, M. J.; Mayer, T. S.; Redwing, J. M.; Robinson, J. A. Highly Scalable, Atomically Thin WSe₂ Grown via Metal–Organic Chemical Vapor Deposition. *ACS Nano* 2015, 9 (2), 2080–2087.
- (22) Lin, Y.-C.; Ghosh, R. K.; Addou, R.; Lu, N.; Eichfeld, S. M.; Zhu, H.; Li, M.-Y.; Peng, X.; Kim, M. J.; Li, L.-J.; Wallace, R. M.; Datta, S.; Robinson, J. A. Atomically Thin Resonant Tunnel Diodes Built from Synthetic van Der Waals Heterostructures. *Nat. Commun.* 2015, 6, 7311.
- (23) Park, J.; Choudhary, N.; Smith, J.; Lee, G.; Kim, M.; Choi, W. Thickness Modulated MoS₂ Grown by Chemical Vapor Deposition for Transparent and Flexible Electronic Devices. *Appl. Phys. Lett.* 2015, 106, 012104.
- (24) Zhan, Y.; Liu, Z.; Najmaei, S.; Ajayan, P. M.; Lou, J. Large-Area Vapor-Phase Growth and Characterization of MoS₂ Atomic Layers on a SiO₂ Substrate. *Small* 2012, 8 (7), 966.
- (25) Han, G. H.; Kybert, N. J.; Naylor, C. H.; Lee, B. S.; Ping, J.; Park, J. H.; Kang, J.; Lee, S. Y.; Lee, Y. H.; Agarwal, R.; Johnson, A. T. Seeded Growth of Highly Crystalline Molybdenum Disulfide Monolayers at Controlled Locations. *Nat. Commun.* 2015, 6, 6128.
- (26) Choi, W.; Choudhary, N.; Han, G. H.; Park, J.; Akinwande, D.; Lee, Y. H. Recent Development of Two-Dimensional Transition Metal Dichalcogenides and Their Applications. *Mater. Today* 2017, 20 (3), 116–130.
- (27) Johnson, D. C. Controlled Synthesis of New Compounds Using Modulated Elemental Reactants. *Curr. Opin. Solid State Mater. Sci.* 1998, 3 (2), 159–167.
- (28) Esters, M.; Johnson, D. C. Targeted Synthesis of Metastable Compounds and Intergrowths: The Modulated Elemental Reactants Method. In *Crystal Growth: Concepts, Mechanisms, and Applications*; Li, J., Li, J., Chi, Y., Eds.; Nova Science Publishers: New York, 2017; pp 35–118.
- (29) Atkins, R.; Wilson, J.; Zschack, P.; Grosse, C.; Neumann, W.; Johnson, D. C. Synthesis of [(SnSe)_{1.15}]_m(TaSe₂)_n Ferecrystals: Structurally Tunable Metallic Compounds. *Chem. Mater.* 2012, 24 (23), 4594–4599.
- (30) Merrill, D. R.; Moore, D. B.; Ditto, J.; Sutherland, D. R.; Falmbigl, M.; Winkler, M.; Pernau, H. F.; Johnson, D. C. The Synthesis, Structure, and Electrical Characterization of (SnSe)_{1.2}TiSe₂. *Eur. J. Inorg. Chem.* 2015, 2015 (1), 83–91.
- (31) Hamann, D. M.; Bardgett, D.; Cordova, D. L. M.; Maynard, L. A.; Hadland, E. C.; Lygo, A. C.; Wood, S. R.; Esters, M.; Johnson, D. C. Sub-Monolayer Accuracy in Determining the Number of Atoms per Unit Area in Ultrathin Films Using X-Ray Fluorescence. *Chem. Mater.* 2018, 30, 6209–6216.
- (32) Wainfan, N.; Parratt, L. G. X-Ray Reflection Studies of the Anneal and Oxidation of Some Thin Solid Films. *J. Appl. Phys.* 1960, 31 (8), 1331–1337.
- (33) Bronsema, K. D.; de Boer, J. L.; Jellinek, F. On the Structure of Molybdenum Diselenide and Disulfide. *Z. Anorg. Allg. Chem.* 1986, 540, 15–17.
- (34) Sathe, D. J.; Chate, P. A. Hexagonal Nanosized Molybdenum Diselenide Thin Film Deposited at 333 K by Chemical Method. *Solid State Sci.* 2015, 48, 19–22.
- (35) Huntley, D. R.; Sienko, M. J.; Hiebl, K. Magnetic Properties of Iron-Intercalated Titanium Diselenide. *J. Solid State Chem.* 1984, 52 (3), 233–243.